Two-Stage Optimal Design of Concentric Ferrite PM Layer IPMSM for Micro-EV Traction Considering Driving Characteristics

Ki-O Kim[1], Du-Ha Park[2], So-Yeon Im[2], Yunyong Choi[3], and Myung-Seop Lim[1]

[1]Department of Automotive Engineering, Hanyang University, Seoul 04763, Republic of Korea
[2]Department of Automotive Engineering (Automotive-Computer Convergence), Hanyang University, Seoul 04763, Republic of Korea
[3]DRIVETECH Company Ltd., Bucheon 14558, Republic of Korea

In this article, the interior permanent magnet synchronous motor (IPMSM) using ferrite permanent magnet (PM) for micro-electric vehicle (EV) traction is proposed. The characteristics of V-type IPMSM using Nd PM and a motor of the same shape using ferrite PM are analyzed when applied to micro-EV traction, the cases of power dissatisfaction with ferrite PM motor are derived, and the improvement methods are presented. Based on the improvement method, the rotor outer diameter, PM layer, and PM ratio are considered in the initial design. After the initial design, a two-stage optimization method is introduced to reduce the number of samples required. The first optimization is performed considering the power of the driving area, mechanical stiffness analysis during high-speed rotation, and low-temperature demagnetization analysis of ferrite PM. Then, the second optimization is performed considering the main operating points (MOPs) of the efficiency perspective and the MOPs of the frequency perspective through micro-EV model. Based on the design results, the possibility of a motor for micro-EV using ferrite PM is suggested by comparing the performance with the existing motor using Nd PM. Experiments are conducted on the manufactured motor, and the validity of the design results is verified by comparing the test results and FEA results.

***Index Terms*— Ferrite permanent magnet (PM), irreversible demagnetization (ID), micro-electric vehicle (EV), optimum design, safety factor (SF), traction motor.**

I. Introduction

MICRO-ELECTRICAL vehicles (EVs) are increasingly positioned as a means for future sustainable personal mobility [1]. To achieve the high performance of micro-EV, various studies have been conducted on interior permanent magnet synchronous motor (IPMSM) with Nd PM [2], [3], [4]. However, Nd PM contains rare-Earth elements, such as dysprosium, it is more expensive than other PMs, and its supply is unstable. Therefore, various studies have been conducted on IPMSM using rare-Earth-free PM [5], [6], [7], [8]. In [5], high magnetic torque can be generated using the magnetic flux concentrated PM type, but it has poor mechanical stress performance; therefore, it is not suitable for a traction motor. In [6], [7], and [8], high reluctance torque can be generated by increasing the difference between d-axis and q-axis inductance using a multilayer PM type, but the risk of irreversible demagnetization (ID) of the PM increases as the number of layers increases. Moreover, in the case of micro-EV traction motors, there are concerns about the risk of the PM ID due to low-voltage and high-current specifications. In addition, most research results on traction motors using rare-Earth-free PM greatly exceed the capacity for micro-EV, and the number of studies on the design of traction motors suitable for micro-EV is insufficient. Therefore, in this article, a motor using ferrite PM suitable for micro-EV traction is proposed. Based on a model that replaced the IPMSM for micro-EV using the existing Nd PM with ferrite PM, the design direction is presented by the specifications of the micro-EV motor. In addition, two-stage optimization can be applied to reduce the number of sample points, which can reduce the computational time required for the design. In addition, in the second optimization, the optimization is performed considering the main operating points (MOPs) from the perspective of energy consumption and driving frequency perspective of the micro-EV traction motor.

Manuscript received 24 March 2024; revised 12 May 2024; accepted 15 May 2024. Date of publication 21 May 2024; date of current version 27 August 2024. Corresponding author: M.-S. Lim (e-mail: myungseop@hanyang.ac.kr).

Color versions of one or more figures in this article are available at https://doi.org/10.1109/TMAG.2024.3403903.

Digital Object Identifier 10.1109/TMAG.2024.3403903

II. Comparison of the Power of Nd PM Motor and Ferrite PM Motor for Micro-EV Traction

Table I shows the specifications of the micro-EV traction design motor. Fig. 1 shows the shape and motor characteristics of the V-type IPMSM for micro-EV using Nd PM and the motor shape and characteristics when the PM is changed to ferrite PM. The stator outer diameter is constant, and the rotor outer diameter to stack length of the Nd PM model is 0.6. In the case of IPMSM using ferrite PM, the stack length is 1.75 times longer than the Nd model to satisfy the maximum torque within the current limit. However, the power is not satisfied from the area before the base speed. To determine the cause of the power dissatisfaction, the load characteristics are shown in Fig. 2 by vector diagrams for the Nd PM model and ferrite PM model. The compared load point is the maximum power point at the base speed of the ferrite PM model. The

TABLE I
MOTOR SPECIFICATION FOR MICRO-EV

Contents	Unit	Value	Note
DC voltage	V_{dc}	66	
Maximum current	A_{rms}	400	
Maximum current density	A_{rms}/mm^2	10	
Maximum power	kW	15	
Maximum torque	Nm	60	
Maximum speed	rpm	7000	
Base speed	rpm	2387	
Pole & Slot number	-	8/12	
Rotor/stator outer diameter ratio	-	0.6	Nd PM model
Nd PM base motor stack length	-	1	Normalized
Nd PM residual induction	T	1.2	20°C
Ferrite PM residual induction	T	0.47	20°C

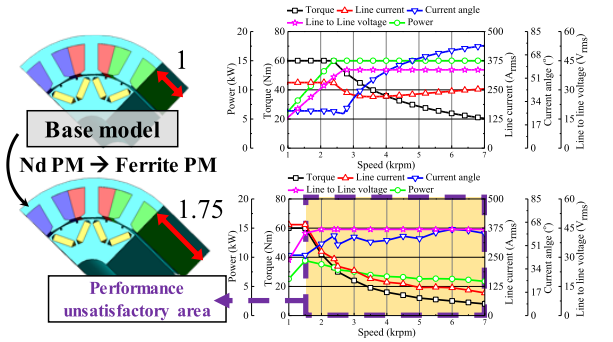

Fig. 1. Shapes and characteristics curves of Nd PM model and ferrite PM model.

red vector is the induced voltage due to magnetic flux linkage caused by the PM field and is significantly smaller in (b) than in (a). Additionally, the blue vector is the induced voltage by inductance, and the voltage component by d-axis inductance is large compared to (b) to (a). Accordingly, the vectors of each induced voltage in (a) and (b) are in the second and third quadrants of the vector diagram. On the other hand, due to the control characteristics of the IPMSM, the vectors of the input current in both (a) and (b) are in the second quadrant. In case (b), as seen in Fig. 1, the current angle for flux weakening control is larger than in (a) due to the increase in voltage as the speed increases. Nevertheless, the phase difference (θ) between the induced voltage and the input current is larger in (b) than in (a). The power factor (PF) is expressed by this phase difference as follows:

$$\mathrm{PF} = \cos\theta \tag{1}$$

where PF is the power factor. The PF of the ferrite PM model is lower than that of the Nd PM model, and this is the cause of output power dissatisfaction as more input power is required to produce the same output. Therefore, the way to satisfy the power by increasing the PF of the ferrite PM motor is to increase the flux linkage by the PM field and reduce the voltage component due to the d-axis inductance. In Section III, the improved design is conducted to improve the flux linkage by the PM field and reduce the d-axis inductance.

III. IMPROVED DESIGN TO INCREASE THE POWER OF IPMSM USING FERRITE PM FOR MICRO-EV TRACTION

The improved design consists of two steps. The first improved design is to increase the PF, and the second is to improve mechanical stability and ID durability.

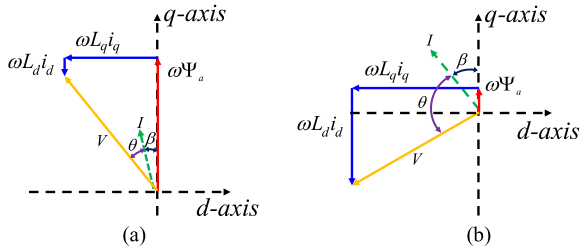

Fig. 2. Vector diagram of (a) Nd PM model and (b) ferrite PM model at the same load point.

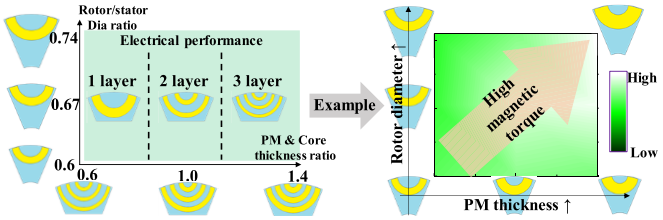

Fig. 3. Classification according to the changes in rotor core and PM.

A. First Improved Design: Increase of PF

As shown in Fig. 3, to improve the PF of a ferrite PM motor, the electrical performances according to the ratio of the outer diameters of the rotor and stator, the number of PM layers, and the ratio of PM and core are reviewed. Electrical performances are calculated based on the maximum current, current phase angle of 0°–90°, maximum torque during 10° step interval, magnetic torque, reluctance torque at this time, and d-axis inductance. In addition, considering the low-temperature ID characteristics of ferrite PM, the ID characteristics are examined under the conditions of 1.2 times the maximum current and a current phase angle of 90° at −40 °C. ID is calculated based on the average demagnetization ratio (DR) for each element of PM as follows:

$$\mathrm{DR}\,(\%) = \left\{1 - \left(\mathrm{Br_{step}}/\mathrm{Br_{org}}\right)\right\} \times 100 \tag{2}$$

where $\mathrm{Br_{step}}$ is the residual flux density during load analysis step, and $\mathrm{Br_{org}}$ is the residual magnetic flux density before analysis. During improved design, the shape of the PM is changed to a concentric C-shape instead of the V-type, which is advantageous for both electrical and mechanical performance [6]. The tendency of magnetic torque according to the thickness ratio of PM and core and rotor/stator diameter ratio at one layer is shown in Fig. 3. As shown in Fig. 4, red boxes are marked for areas that can be improved for each electrical performance. Accordingly, the rotor shape of the improved design was selected as the rotor/stator outer diameter ratio of 0.67, the number of PM layers as 1, and the thickness ratio of PM and core as 1.4.

B. Second Improved Design: Increase Mechanical Stability and ID Durability

Motors for micro-EV traction must ensure mechanical stability even when driven at high speeds. Mechanical stability is judged based on the safety factor (SF), which is the ratio of the maximum stress to the yield strength of the electrical steel. When the SF was 1.2 or more at a rotation speed of 1.2 times the maximum speed, it was considered mechanically

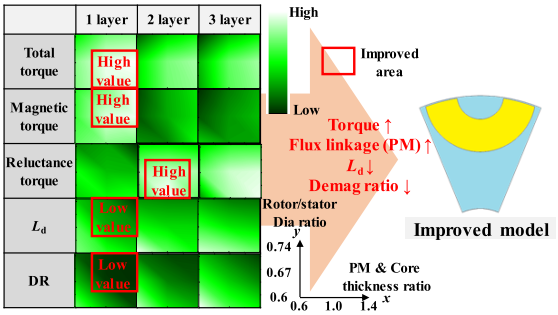

Fig. 4. Electromagnetic performance changes and improvement model shape according to the changes in rotor core and PM shape.

TABLE II
MATERIAL PROPERTIES FOR STRUCTURAL ANALYSIS

Contents	Unit	Core (35PN230)	PM (Ferrite)
Density	kg/m^3	7600	5100
Yield stress	MPa	380	276
Poisson's ratio	-	0.3	0.25
Young's modulus	GPa	175	150

stable [8]. Table II lists the mechanical characteristics of the core and PM. Fig. 5 shows the boundary conditions for structural analysis, the result, and the demagnetization analysis result of the improved model. As a result, the SF was 0.26, which is mechanically unstable, and local ID occurred in PM areas. To improve mechanical stability and prevent ID, a core bridge was inserted at the center of the PM, and a flux barrier was inserted at each end of PM. Fig. 6(a) and (b) shows the result of the second improved design shape and characteristics analysis, and the output was satisfactory in all areas. Additionally, as shown in Fig. 6(c)–(e), the PF increased compared to the initial ferrite PM model at the same load point, mechanical stability was secured with an SF of over 1.8, and no ID occurred. However, as shown in Fig. 6(f), the torque ripple was 73.0% and 77.7% at the maximum output load at the base and max speeds, respectively. Additionally, as shown in Fig. 6(g), the peak value of line-to-line induced voltage at the max speed load was 149.1V_{peak}, which is higher than the dc input voltage of 66.0 V. In addition, the current density at maximum torque was 13 $A_{\text{rms}}/\text{mm}^2$, which exceeds the limit of 10 $A_{\text{rms}}/\text{mm}^2$. In Section IV, the optimization for current density, torque ripple, and induced voltage reduction is carried out step by step, and the MOPs in terms of the efficiency and frequency of the micro-EV drive motor are considered.

IV. TWO-STAGE OPTIMAL DESIGN OF MOTOR FOR DRIVING MICRO-EV

Section III required reductions in current density, torque ripple, and line-to-line induced voltage. It is possible to simultaneously maximize torque to reduce current density and minimize torque ripple and line-to-line induced voltage. However, in this case, as the design variables increases, the number of experimental points may become excessively large to achieve reliability. In the case of simultaneous optimization, the number of design variables required is 22, and in the case of stepwise optimization, the number of design variables required is 12 and 11, respectively. N_s is the number of

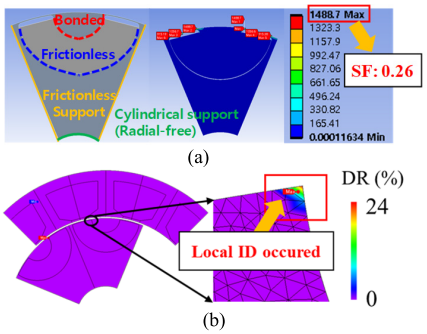

Fig. 5. Boundary conditions for structural analysis and result and the demagnetization analysis result of the improve model. (a) Structure analysis. (b) Demagnetization analysis.

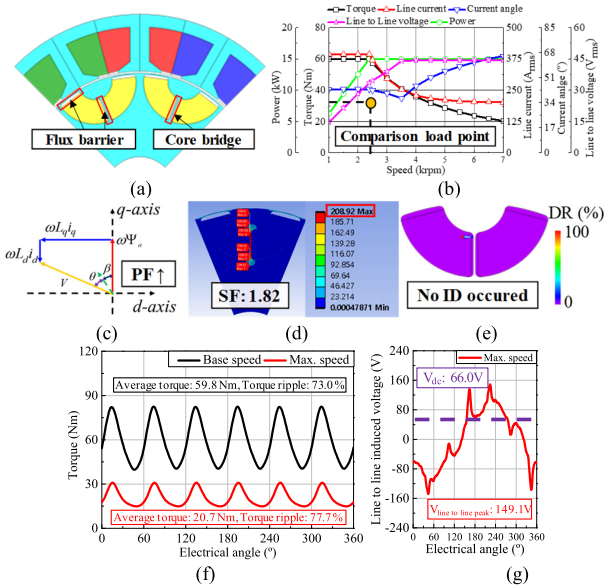

Fig. 6. Second improved design shape and characteristics. (a) Shape. (b) Characteristic curves. (c) Vector diagram. (d) Structure analysis result. (e) Demagnetization analysis result. (f) Load torque (base and max point). (g) Line-to-line induced voltage at max speed point.

samples required for optimization according to design variables and is expressed as follows [4]:

$$N_s = \frac{(N_{\text{dv}} + 1)(N_{\text{dv}} + 2)}{2} \tag{3}$$

where N_{dv} is the number of design variables. As shown in Fig. 7, two-stage optimization can reduce the number of sample points. In each stage of optimization, a genetic algorithm based on the kriging surrogate model is used [8]. The kriging surrogate model-based optimization is used in motor optimal design because it has high accuracy in predicting nonlinearity that reflects the magnetic saturation characteristics of the motor [4].

A. First Optimization: Maximize Torque

In the first optimization, an objective function is selected to maximize torque to reduce the current density within the limiting conditions. Constraints are torque to satisfy power at maximum speed and current density less than 10 $A_{\text{rms}}/\text{mm}^2$. Additionally, for mechanical stability, the maximum stress is 320 MPa or less, and to prevent ID of PM at low temperature, the PM DR is set at 0%. The first optimization

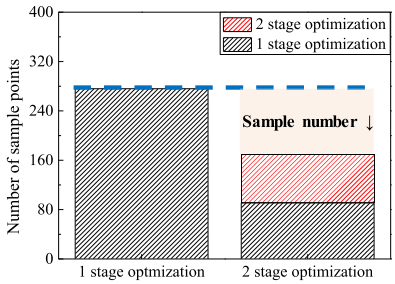

Fig. 7. Comparison of number of sample points.

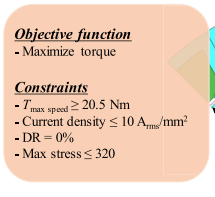

Notation	Design variables	Unit	Min	Max
X1	Rotor Outer radius	mm	47	52
X2	Core ratio	-	0.2	0.5
X3	Core bridge thickness	mm	0.5	1.2
X4	PM fillet upper radius	mm	0.5	1.5
X5	PM fillet lower radius	mm	0.5	1.5
X6	PM offset	mm	0.5	1
X7	PM distance	mm	0.5	1
X8	Tooth width	mm	8	12
X9	Yoke width	mm	4	8
X10	Slot opening width	mm	4	9
X11	Tooth tip thickness	mm	1	2
X12	Turns per slot	-	12	28

Fig. 8. First-stage optimization conditions and design variables.

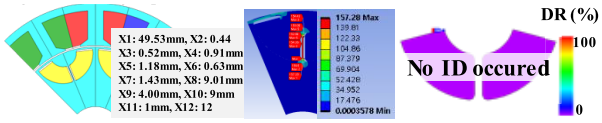

Fig. 9. First-stage optimization results. (a) Design variables. (b) Structure and demagnetization analysis results.

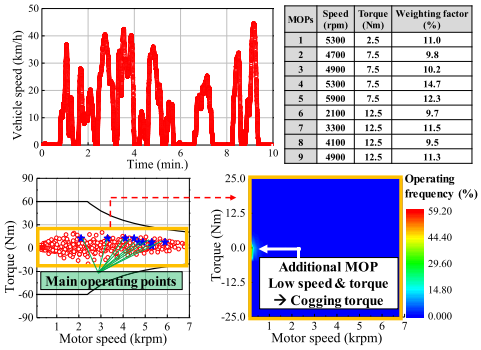

MOPs	Speed (rpm)	Torque (Nm)	Weighting factor (%)
1	5300	2.5	11.0
2	4700	7.5	9.8
3	4900	7.5	10.2
4	5300	7.5	14.7
5	5900	7.5	12.3
6	2100	12.5	9.7
7	3300	12.5	11.5
8	4100	12.5	9.5
9	4900	12.5	11.3

Fig. 10. Driving cycle of the micro-EV and the resulting MOPs of the motor.

conditions and design variables are shown in Fig. 8. As a result of the first optimization, the maximum torque could not be satisfied under the current density within 10 A_{rms}/mm^2. Therefore, to satisfy the maximum torque, the stack length was increased by 1.46 times compared to Nd model. The first optimal model satisfied the power in all areas, and as shown in Fig. 9, mechanical stability was secured, and ID did not occur. However, torque ripple at maximum load at base speed and max speed was not significantly improved at 67.1% and 58.5%, respectively.

B. Second Optimization: Minimize Torque Ripple and Performance Optimization About MOPs

In the second optimization, the stator chamfer and rotor notch are applied as design variables to reduce torque ripple. In addition, the thickness of the rotor rib is applied to compensate for the resulting decrease in the fundamental component of the flux linkage. Additionally, to maximize the performance of a micro-EV traction motor, the performance improvement of the motor's MOPs from an efficiency and

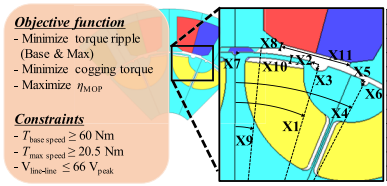

Notation	Design variables	Unit	Min	Max
X1	Notch 1 angle	°	15	20
X2	Notch 1 major radius	mm	0.5	1.7
X3	Notch 1 minor radius	mm	0.5	2.3
X4	Notch 2 angle	mm	25	30
X5	Notch 2 major radius	°	0.5	1.7
X6	Notch 2 minor radius	mm	0.5	2.3
X7	Notch 3 radius	mm	0.35	1.5
X8	Stator chamfer	mm	0.5	1
X9	Stator chamfer angle	°	1	8
X10	Rotor rib thickness	mm	0.5	1
X11	Stator slot opening	mm	6	12

Fig. 11. Second-stage optimization conditions and design variables.

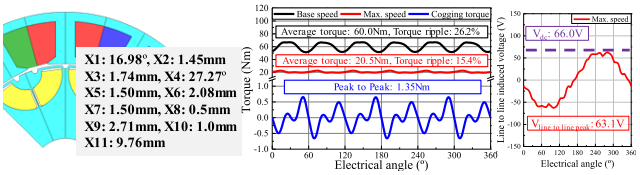

Fig. 12. Second-stage optimization results. (a) Design variables. (b) Load torque (base and max speed) and cogging torque. (c) Line-to-line induced voltage at max speed point.

frequency perspective is reflected in the objective function. The MOPs of the traction motor were determined by modeling the micro-EV [4]. The target driving cycle was the New York City Cycle (NYCC). The MOPs are considered the MOPs with an energy consumption rate of 3.5% or more from an efficiency perspective and the maximum operating frequency area from a frequency perspective. Accordingly, a total of MOPs was adopted from an efficiency perspective and a frequency perspective, and an additional goal was to reduce cogging torque as a representative value, as the operating frequency is highest in the low-speed, low-torque area. Fig. 10 shows the driving cycle of the micro-EV and the resulting MOPs of the motor. The weighting factors in Fig. 10 are determined according to the ratio of each MOP to the sum of the energy consumption ratios of the MOPs. The main driving efficiency of the micro-EV traction motor calculated by multiplying the efficiency of the corresponding MOP by the weighting factor is as follows [4]:

$$\eta_{\mathrm{MOP}} = \sum_{i=1}^{9} \eta_i w_i \tag{4}$$

where η_i is the motor efficiency and w_i is the weight factor at the ith MOP. The second optimization conditions and design variables are shown in Fig. 11. Based on the second optimization results, the stack length was increased to 1.55 times that of the Nd model to satisfy the maximum torque under limited current density condition. The second optimal model satisfied the power in all areas, and as shown in Fig. 12, the torque ripple of the target load at each base and max speed was 26.2% and 15.4%, respectively, and the cogging torque was 1.35 N·m. For additional torque ripple and cogging torque reduction, a two-step skew was applied to the rotor and a skew angle between the steps of 7.5°, which can reduce the fundamental value of cogging torque. The decrease in average torque due to the skew was compensated for by increasing stack length to 1.64 times that of the Nd model. The results of the shape, electromagnetic properties, stress distribution, and ID analysis results for the final models are shown in Fig. 13. As with the results of the second optimal design, the power was satisfactory for all areas, it was mechanically stable, and no ID occurred. In addition, compared to the second optimal design

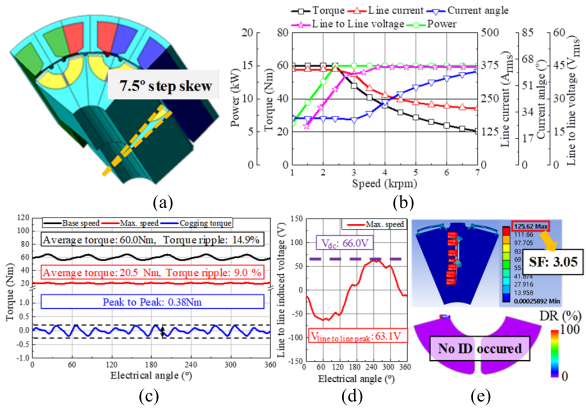

Fig. 13. Final model design results. (a) Shape. (b) Characteristics curves. (c) Load torque (base and max speed) and cogging torque. (d) Line-to-line induced voltage at max speed point. (e) Structure and demagnetization analysis results.

TABLE III
MOPs LOAD TEST AND FEA COMPARISON RESULTS

MOPs	Speed (rpm)	Torque (Nm)	FEA current (Arms)	Exp. current (Arms)	Error (%)
1	5300	2.5	23.87	23.37	2.07
2	4700	7.5	62.40	60.0	3.84
3	4900	7.5	62.45	60.10	3.77
4	5300	7.5	62.68	61.30	2.21
5	5900	7.5	64.78	66.90	-3.27
6	2100	12.5	95.87	95.05	0.85
7	3300	12.5	96.14	98.63	-2.59
8	4100	12.5	96.38	97.80	-1.47
9	4900	12.5	97.94	97.86	0.08

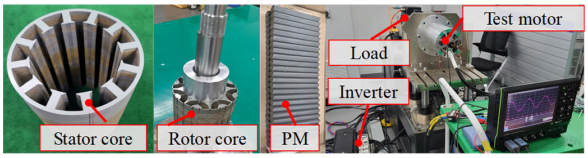

Fig. 14. Fabricated stator and rotor cores, ferrite PMs, and test setup.

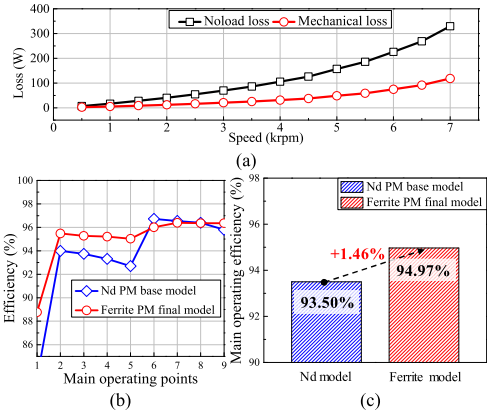

Fig. 15. No-load test and comparison of MOP efficiency. (a) No-load test. (b) Comparison for each main operating efficiency point. (c) Comparison of main operating efficiency of micro-EV traction motor.

result, the torque ripple during load at each base speed and max speed decreased, and the cogging torque also decreased.

V. VERIFICATION

To validate the design of the micro-EV traction using ferrite PM, the final model was built and tested. Fig. 14 shows the fabricated stator and rotor cores, ferrite PMs, and test setup. The results of the no-load loss according to speed and the mechanical loss, which is the loss when the no-load iron loss is exclude, are shown in Fig. 15(a). Since then, no-load at the max speed of 7000 r/min was tested stably, and the mechanical stability at 7000 r/min was verified. Table III shows the data comparing test and finite element analysis (FEA) results for the MOPs. At all test points, the current error between the test and FEA results was less than 4%. From these test results, the FEA of the final model is well analyzed. Hence, the comparison of the characteristics of Nd model and final model was also well analyzed. The efficiency at each MOPs of the Nd model and the ferrite PM optimal model is shown in Fig. 15(b), and the efficiency at the MOPs of traction motor with the weight factor reflected is shown in Fig. 15(c). As shown in Fig. 15(b) and (c), the efficiency of the MOPs for micro-EV traction in the ferrite PM model was 1.46% greater.

VI. CONCLUSION

In this article, a design that replaces Nd PM with ferrite PM in IPMSM for micro-EV traction is proposed. The causes of output dissatisfaction with the ferrite PM model were analyzed and improvement design was performed. The optimal design was divided into two stages and design variables appropriate for the purpose were selected to reduce the number of sample points. For micro-EV traction drives, the optimal design was carried out to adopt and improve the MOPs in terms of efficiency and frequency. As a result, efficiency at the MOPs for micro-EV traction was improved compared to the Nd model. Therefore, it is concluded that the proposed motor design method for micro-EV traction using ferrite PM is valid.

ACKNOWLEDGMENT

This work was supported by the Competency Development Program for Industry Specialist, Korea Institute for Advancement of Technology (KIAT) by the Korea Government (MOTIE), under Grant P0017120.

REFERENCES

[1] X. Liu, H. Chen, J. Zhao, and A. Belahcen, "Research on the performances and parameters of interior PMSM used for electric vehicles," *IEEE Trans. Ind. Electron.*, vol. 63, no. 6, pp. 3533–3545, Jun. 2016.

[2] X. Sun, Z. Shi, G. Lei, Y. Guo, and J. Zhu, "Analysis and design optimization of a permanent magnet synchronous motor for a campus patrol electric vehicle," *IEEE Trans. Veh. Technol.*, vol. 68, no. 11, pp. 10535–10544, Nov. 2019.

[3] F. Ma, H. Yin, L. Wei, G. Tian, and H. Gao, "Design and optimization of IPM motor considering flux weakening capability and vibration for electric vehicle applications," *Sustainability*, vol. 10, no. 5, May 2018, Art. no. 1533.

[4] S.-Y. Im, K.-S. Cha, Y.-J. Won, Y.-Y. Choi, and M.-S. Lim, "Two-step optimum design process of PMSM to improve driving efficiency and harmonics of lightweight electric vehicle," *IEEE Trans. Ind. Appl.*, vol. 59, no. 6, pp. 6685–6694, Nov. 2023.

[5] M.-R. Park, J.-W. Jung, D.-Y. Kim, J.-P. Hong, and M.-S. Lim, "Design of high torque density multi-core concentrated flux-type synchronous motors considering vibration characteristics," *IEEE Trans. Ind. Appl.*, vol. 55, no. 2, pp. 1351–1359, Mar. 2019.

[6] Y.-H. Jung, M.-R. Park, K.-O. Kim, J.-W. Chin, J.-P. Hong, and M.-S. Lim, "Design of high-speed multilayer IPMSM using ferrite PM for EV traction considering mechanical and electrical characteristics," *IEEE Trans. Ind. Appl.*, vol. 57, no. 1, pp. 327–339, Jan. 2021.

[7] E. Sayed et al., "Design of multilayer concentric ferrite-magnet machines for a traction application," *IEEE Trans. Transport. Electrific.*, vol. 7, no. 3, pp. 1548–1560, Sep. 2021.

[8] K.-O. Kim, Y.-H. Jung, J.-C. Park, and M.-S. Lim, "Comparative study of mechanical and electrical characteristics of high-strength and conventional electrical steel for EV traction high-speed multilayer IPMSM using rare-Earth free PM," *IEEE Trans. Magn.*, vol. 59, no. 11, pp. 1–5, Nov. 2023.